SUPPORTING INFORMATION

Plasmonic biocompatible silver-gold alloyed nanoparticles

Georgios A. Sotiriou[1,2], Gion Diego Etterlin[1], Anastasia Spyrogianni[1], Frank Krumeich[1], Jean-Christophe Leroux[3], Sotiris E. Pratsinis[1]*

[1]Particle Technology Laboratory, Institute of Process Engineering, Department of Mechanical and Process Engineering, ETH Zurich, Sonneggstrasse 3, Zurich 8092, Switzerland.
[2]Molecular and Integrative Physiological Sciences, Department of Environmental Health, School of Public Health, Harvard University, 665 Huntington Ave., Boston, MA 02115, USA.
[3]Drug Formulation & Delivery, Institute of Pharmaceutical Sciences, Department of Chemistry and Applied Biosciences, ETH Zurich, Vladimir-Prelog-Weg 3, Zurich 8093, Switzerland.

Chemical Communications

*Corresponding author: sotiris.pratsinis@ptl.mavt.ethz.ch

Materials and Methods

Gold-silver nanoparticles on nanostructured silica support were made by an open flame-spray-pyrolysis (FSP) reactor, described in detail elsewhere. In brief, appropriate amounts of silver acetate (Sigma Aldrich, purity >99%) and/or gold acetate (Alfa Aesar, purity 99.9%) were dissolved in 1:1 mixture of 2-ethylhexanoic acid (Sigma Aldrich, purity >98%) and acetonitrile (Sigma Aldrich, purity >98%) keeping the noble metal concentration at 0.15 M. Afterwards hexamethyldisiloxane (HMDSO, Sigma Aldrich, purity >97%) was added in the solution corresponding to 50 wt% SiO_2 in the final nanoparticle composition. Then the solution was stirred and heated up to a temperature of 100 °C in oil bath for at least half an hour before fed to the FSP nozzle (5 mL/min) and atomized by 5 L/min O_2 (Pan Gas, purity >99.9%).

Scanning transmission electron microscopy (STEM) studies were performed using an aberration-corrected, dedicated STEM (Hitachi HD-2700CS) apparatus equipped with a probe corrector (CEOS). STEM was performed at an acceleration potential of 200 kV (electron gun: cold-field emitter) in the ultra-high resolution mode of this microscope (Inada et al., 2009, Krumeich et al., 2011). Various detectors can be chosen for imaging in bright-field (BF) and dark-field modes (HAADF). The collection angle in BF mode is selected in such a way that the direct beam and the diffracted beams interfere with one another, generating an interference pattern (phase contrast) (Krumeich et al., 2013). A secondary electron detector and an EDX spectrometer (Gemini system, EDAX) were mounted in the electron column above the sample.

X-ray diffraction (XRD) patterns were performed with a Bruker D8 advance diffractometer (40 kV,40 mA, CuKα radiation) at 2θ=15-70° with a step size of 0.0145°. The crystallite sizes were obtained by refined Rietveld Analysis on the (111) peak of Au-Ag using the TOPAS 4 software. The ultraviolet-visible spectroscopy (UV-vis) optical absorption spectra were obtained with a Cary Varian 500 from 250 nm to 800 nm with a step size of 0.333 nm. Particles were dispersed in water at a concentration of 0.02 mg/mL by ultrasonication (Sonics vibra cells 600 W, 2 min, 1s on/1s off pulse, 70% power). The Ag^+ ion concentration of aqueous suspensions containing the Ag-Au/SiO_2

nanoparticles was measured with an ion selective electrode and an ion meter (both Metrohm). The concentration of the particles dispersed in water for the Ag^+ ion release measuring was 100 mg/L. Photothermal heating measurements were performed using a Sloc laser with a wavelength of 785 nm to irradiate the samples. To measure the temperature raise a thermal imager of type Fluke Ti110 was used. For this, 10 mg Ag-Au/SiO_2 nanoparticles were mixed with 200 mg pure KBr powder using a mortar and pressed to a pill (d = 13 mm). X-ray photoelectron spectroscopy was performed with a Thermo Scientific K-Alpha spectrometer.

Nanoparticle suspensions for their cytotoxicity evaluation were first prepared in fresh ultrapure water (Milli-Q®, 18.2 MΩ·cm, 25^{o}C, TOC: 3 ppb) at a metal (Ag-Au) concentration of 100 mg/L. So, 2 mg of each nanoparticles were dispersed in 10 mL of water in conical polystyrene tubes (tube size: 50 mL), followed be intense vortex-mixing and ultrasonication, using a water-cooled high intensity cup horn system (VCX500, cup horn Part no. 630-0431, Sonics Vibracell). Ultrasonic energy (50 kJ) was provided in pulses (30 s on, 1 s off) at 95% amplitude and the total liquid volume (volume of the cooling water any time in the cup plus suspension volume) was approximately 0.5 L. All suspensions were transferred in glass vials directly after ultrasonication to be steam-sterilized, using a Tuttnauer, 2540 EL Benchtop autoclave (liquids program, 121 ^{o}C for 20 min). After steam-sterilization, the suspensions were diluted with serum-free cell culture medium without phenol red (DMEM, High Glucose, no Glutamine, no Phenol Red supplemented with 1% PenStrep, 1% Sodium Pyruvate 100 mM Solution and 2% GlutaMAX^{TM}, all from Invitrogen) at a volume ratio 1:3, under sterile conditions (in laminar air flow hood). Therefore, similarly sterilized fresh ultrapure water was also used to achieve the desired concentrations. Nanoparticle-free solutions were prepared by mixing steam-sterilized ultrapure water with serum-free medium at a volume ratio of 1:3.

RAW 264.7 murine macrophages were cultured in Dulbecco's Modified Eagle medium with phenol red (DMEM, High Glucose, GlutaMAX™, Pyruvate, Invitrogen) supplemented with 1% PenicillinStreptomycin Solution (PenStrep, Invitrogen) and 10% Foetal Bovine Serum (FBS,

Invitrogen) at standard incubation conditions, *i.e.* 37 °C in a humidified atmosphere containing 5% CO_2 (Pratsinis et al., 2013). Subcultivation was performed every 2-3 days.

In vitro cell viability in terms of cell mitochondrial activity was determined by the MTS Assay (Pratsinis et al., 2013). The cytotoxicity of nanosilver particles of these sizes (~10 nm) originates mostly from the released Ag^+ ions from their oxidized surface (Pratsinis et al., 2013). Therefore, it is anticipated that the cytotoxicity of the nanoalloys should progressively decrease with an increase in the Au content. This is examined here against murine macrophages that serve as a model cell line since these cells will be likely the most exposed to nanoparticles following systemic exposure in mammals. Nanoparticles are generally cleared from the systemic circulation by the mononuclear phagocyte system.

RAW 264.7 macrophages in serum-containing medium (10% FBS) without phenol red (DMEM, High Glucose, no Glutamine, no Phenol Red supplemented with 1% PenStrep, 1% Sodium Pyruvate 100 mM Solution and 2% GlutaMAX^{TM}, all from Invitrogen) were seeded in a 96-well plate (100 μL per well) at a concentration of 12'500 cells/well and cultured for 24 h at standard incubation conditions. Then, the medium in each well was exchanged with 100 μL of nanoparticle suspensions in serum-free medium without phenol red, followed by 24 h incubation. Such nanoparticle suspensions were also added in wells without cells to obtain background measurements for each concentration. Cells treated with nanoparticle-free dispersions were used as negative control. Then, 20 μL of MTS were added in each well to be incubated for 2 h. The absorption at 490 nm was measured using a plate reader (Tecan Infinite M200 PRO). For each concentration 5 replicate measurements (and 2 replicate background measurements) were performed per experiment and, at least, three independent experiments (with cells in different passages) were conducted. The absorption of each well containing cells was blank corrected (Brulisauer et al., 2012), by subtracting the average absorption of the corresponding background wells, and expressed as percentage of the (blank corrected) average absorption value of the control cells. This percentage was defined as the relative cell viability (or cell viability, %). The final cell

viability is given as arithmetic mean ± standard deviation of the independent sets of replicate measurements.

Results

Nanostructured SiO_2 particles are formed first in the flame followed by the metallic nanoparticles due to the higher boiling point of SiO_2 than those of both gold and silver. Figure S1 shows the metallic particle size distributions as determined by the electron microscopy for 0 at% Au (a, pure Ag), 20 (b), 30 (c), 50 (d) and 100 at% Au (e, pure Au) along with their average size d_p, geometric standard deviation σ_g, and the total number of counted particles N. The solid line shows the lognormal fit of the size distributions. All samples exhibit a unimodal size distribution with sizes ranging from 5-12 nm, while their s_g are in agreement to similarly flame-made Ag nanoparticles on SiO_2.

The crystallinity of the as-prepared nanoalloys was evaluated by X-ray diffraction (XRD) as shown in Figure S2a. For all samples, the XRD peak positions are identical independent from the Au content at%. This is attributed to the almost same lattice constant of silver and gold (0.408 and 0.409 nm, respectively). Furthermore, the XRD peaks broaden upon the Au addition, further indicating the decrease in nanoalloy size. In contrast, the XRD peaks of the pure Au nanoparticles are sharper further indicating their larger size. Upon the Rietveld analysis of these main diffraction peaks, the average nanocrystal size is calculated and shown in Figure S2b (d_{XRD}, triangles), along with the average particle size from the electron microscopy analysis (d_{TEM}, circles). Both average sizes practically overlap indicating that the nanoalloys are single-crystalline, similarly to similarly-made nanosilver particles (Sotiriou and Pratsinis, 2010). It should be noted that the Rietveld analysis of the patterns for Au content 30, 50 and 75 at% reveals that there is a slight bimodality for these metallic crystal sizes (Sotiriou et al., 2011). More specifically, if the patterns are fitted with two crystal sizes the large crystal size (d_{XRD} = 15 nm) fractions correspond to <5 wt%. This

bimodality might originate from the liquid precursor instability and compatibility, since some precursor precipitation was observed for high Au acetate concentrations.

Figure S3 shows the Ag^+ ion release % (Ag as Ag^+ ions, normalized to the total Ag content) for all Ag-Au nanoalloys (0-75 at% Au, open symbols). If the alloying with Au would have no effect on the Ag^+ ion release, all nanoalloys should exhibit similar values. However, the Ag^+ ion release obtains minimal values for increasing Au content. In contrast, the mechanically-mixed Ag-Au samples (filled symbols) retain their high Ag^+ ion release %.

Figure S4 shows the binding energy (BE) spectra of Ag3$d_{5/2}$ and Ag3$d_{3/2}$ (a) from Ag-Au nanoalloys (0-75 at% Au content) and the Ag3$d_{5/2}$ BE as a function of Au content (b). The BE of pure Ag is slightly higher than its bulk counterpart (Wang et al., 2005a). This has been observed for noble metals supported on ceramics such as SiO_2 and attributed to interactions between the support and the noble metal (Wang et al., 2005b). The Ag3*d* BE slightly increases (> 0.1 eV) for 10 at% Au content. Even though such a small increase might not be significant, a perturbation of the Ag electronic state due to the Au presence is possible. For increasing Au content, however, the Ag3*d* BE monotonically decreases and has been attributed to the charge transfer between Au and Ag atoms (Qu et al., 2013, Wang et al., 2005b). The Ag3*d* BE negative shift may also be attributed to the large difference in the electron structures of Ag atoms between pure Ag and Au-Ag particles, which have different coordination environments (Huang et al., 2013). Similarly, the Au4*f* BE increases for increasing Ag content, further indicating the nanoalloy formation. Figure S4 also shows the binding energy (BE) spectra of Au4*f* (c) from all Ag-Au nanoalloys and the Au4*f* BE as a function of Au content (d). The BE of the Au4*f* BE that shifts to higher values for an increasing Ag content, further indicating the nanoalloy formation (Huang et al., 2013).

Figure S5 shows the cell viability of all Ag-Au nanoalloys as a function of Ag mass concentration. At similar Ag mass concentrations, the Ag-Au nanoalloys exhibit higher cell viability values than that of pure Ag. This highlights that the cytotoxicity of nanosilver can be

drastically controlled by Au nanoalloying that minimizes the surface oxide formation and subsequent Ag^+ ion release.

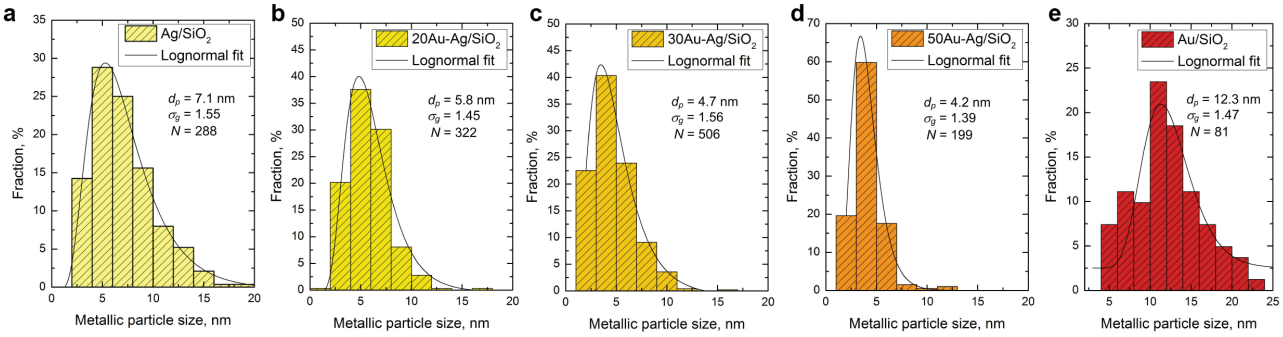

Figure S1. The metallic particle size distributions as determined by the electron microscopy for 0 at% Au (a, pure Ag), 20 (b), 30 (c), 50 (d) and 100 at% Au (e, pure Au) along with their average size d_p, geometric standard deviation σ_g, and the total number of counted particles N. The solid line shows the lognormal fit of the size distributions.

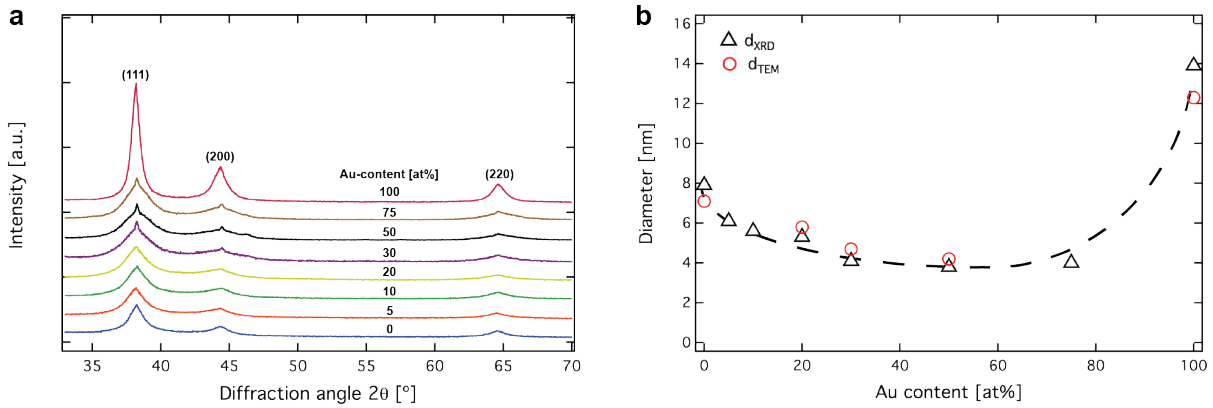

Figure S2. (a) X-ray diffraction (XRD) patterns of all nanoalloys (0-100 at% Au content). (b) The average metallic crystal size (triangles) and primary particle size (circles) as determined from the XRD patterns and the electron microscopy analysis, respectively.

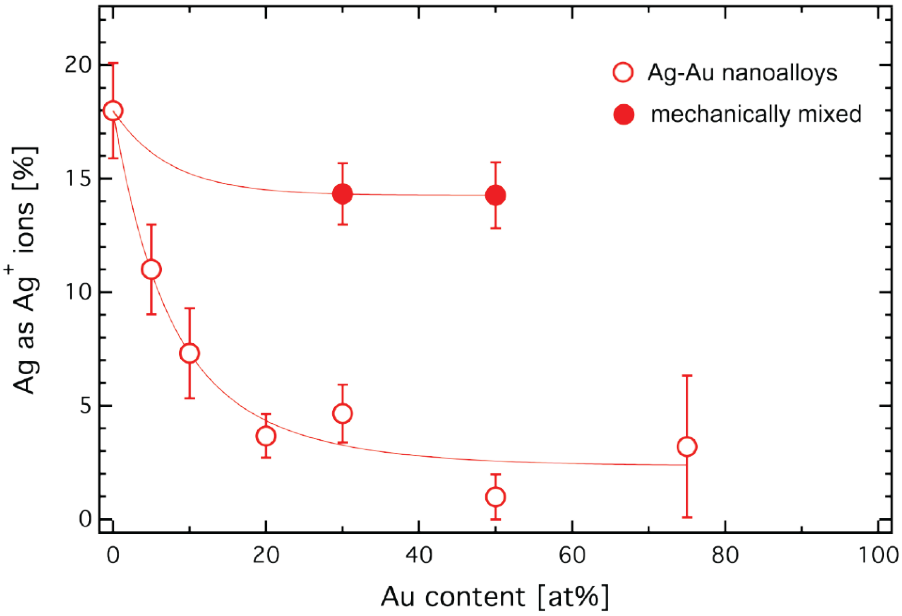

Figure S3. Ag^+ ion release % normalized to the total Ag content as a function of Au content in the Ag-Au nanoalloys (open symbols) and the mechanically-mixed Ag-Au nanoparticles (filled symbols).

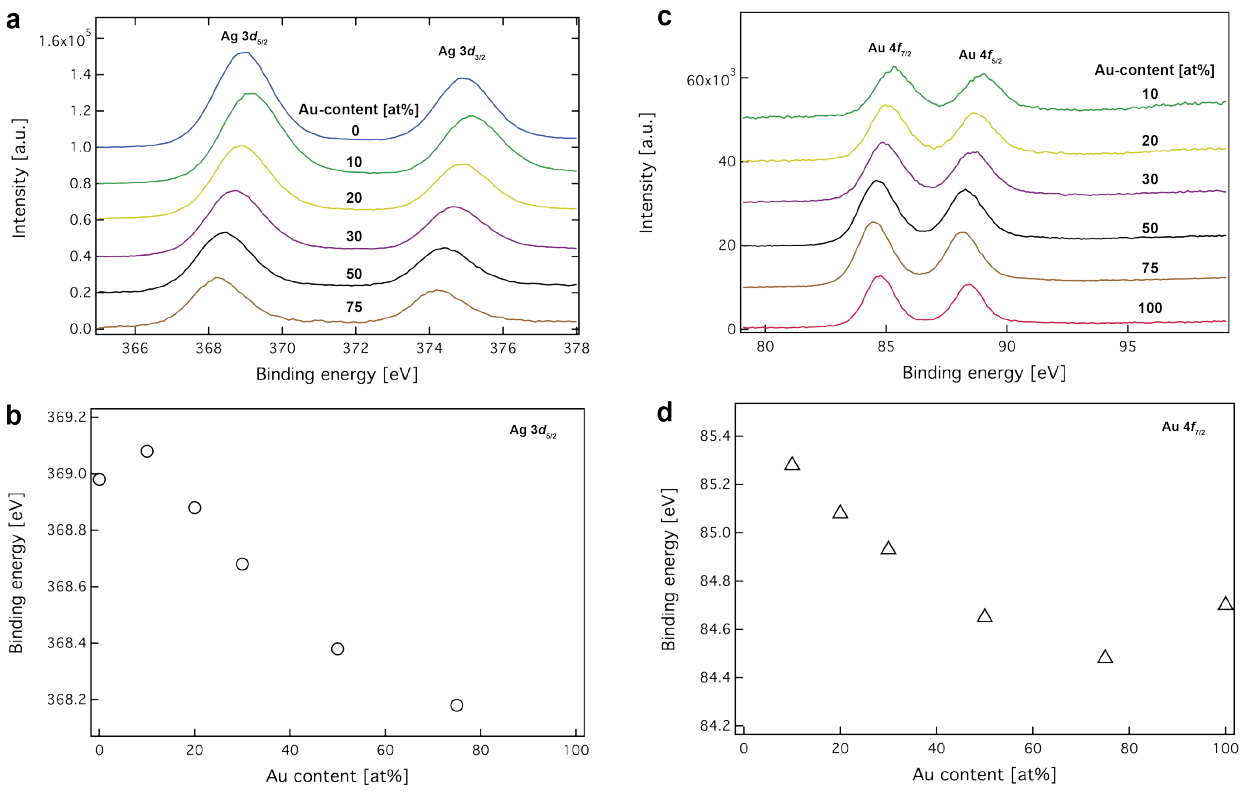

Figure S4. (a) The binding energy (BE) spectra of Ag3$d_{5/2}$ and Ag3$d_{3/2}$ from Ag-Au nanoalloys (0-75 at% Au content) and (b) the Ag3$d_{5/2}$ BE as a function of Au content. (c) The binding energy (BE) spectra of Au4*f* from Ag-Au nanoalloys (10-100 at% Au content) and (d) the Au4*f* BE as a function of Au content.

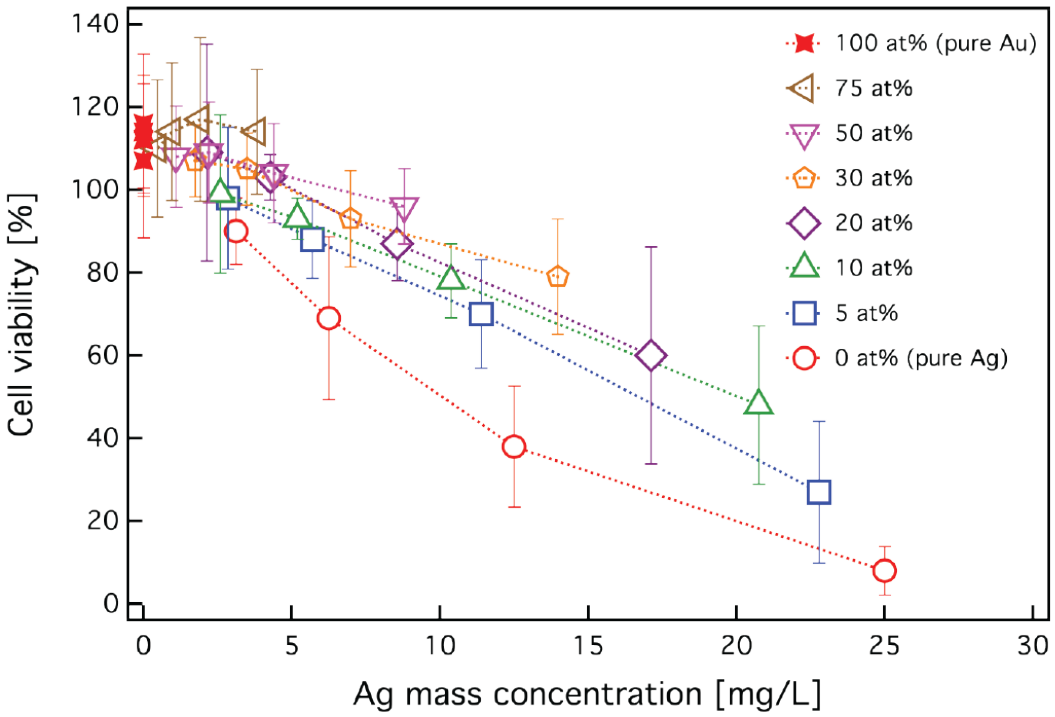

Figure S5. Cell viability of all Ag-Au nanoalloys as a function of Ag mass concentration.

References

BRULISAUER, L., KATHRINER, N., PRENRECAJ, M., GAUTHIER, M. A. & LEROUX, J. C. 2012. Tracking the Bioreduction of Disulfide-Containing Cationic Dendrimers. *Angewandte Chemie-International Edition,* **51,** 12454-12458.

HUANG, X., WANG, X., WANG, X., WANG, X., TAN, M., DING, W. & LU, X. 2013. P123-stabilized Au-Ag alloy nanoparticles for kinetics of aerobic oxidation of benzyl alcohol in aqueous solution. *Journal of Catalysis,* **301,** 217-226.

INADA, H., WU, L., WALL, J., SU, D. & ZHU, Y. 2009. Performance and image analysis of the aberration-corrected Hitachi HD-2700C STEM. *Journal of Electron Microscopy,* **58,** 111-122.

KRUMEICH, F., MUELLER, E. & WEPF, R. A. 2013. Phase-contrast imaging in aberration-corrected scanning transmission electron microscopy. *Micron,* **49,** 1-14.

KRUMEICH, F., MUELLER, E., WEPF, R. A. & NESPER, R. 2011. Characterization of Catalysts in an Aberration-Corrected Scanning Transmission Electron Microscope. *Journal of Physical Chemistry C,* **115,** 1080-1083.

PRATSINIS, A., HERVELLA, P., LEROUX, J.-C., PRATSINIS, S. E. & SOTIRIOU, G. A. 2013. Toxicity of Silver Nanoparticles in Macrophages. *Small,* **9,** 2576-2584.

QU, Z., KE, G., WANG, Y., LIU, M., JIANG, T. & GAO, J. 2013. Investigation of factors influencing the catalytic performance of CO oxidation over Au-Ag/SBA-15 catalyst. *Applied Surface Science,* **277,** 293-301.

SOTIRIOU, G. A. & PRATSINIS, S. E. 2010. Antibacterial activity of nanosilver ions and particles. *Environmental Science & Technology,* **44,** 5649-5654.

SOTIRIOU, G. A., TELEKI, A., CAMENZIND, A., KRUMEICH, F., MEYER, A., PANKE, S. & PRATSINIS, S. E. 2011. Nanosilver on nanostructured silica: Antibacterial activity and Ag surface area. *Chemical Engineering Journal,* **170,** 547-554.

WANG, A. Q., CHANG, C. M. & MOU, C. Y. 2005a. Evolution of catalytic activity of Au-Ag bimetallic nanoparticles on mesoporous support for CO oxidation. *Journal of Physical Chemistry B,* **109,** 18860-18867.

WANG, A. Q., LIU, J. H., LIN, S. D., LIN, T. S. & MOU, C. Y. 2005b. A novel efficient Au-Ag alloy catalyst system: preparation, activity, and characterization. *Journal of Catalysis,* **233,** 186-197.